

# An integrated platform for live 3D human reconstruction and motion capturing

Dimitrios S. Alexiadis, Anargyros Chatzitofis, Nikolaos Zioulis,  
Olga Zoidi, Georgios Louizis, Dimitrios Zarpalas and Petros Daras, *Senior Member, IEEE*

**Abstract**—The latest developments in 3D capturing, processing and rendering provide means to unlock novel 3D application pathways. The main elements of an integrated platform, which target Tele-Immersion (TI) and future 3D applications, are described in this paper, addressing the tasks of real-time capturing, robust 3D human shape/appearance reconstruction and skeleton-based motion tracking. More specifically, initially the details of a multiple RGB-D capturing system are given, along with a novel sensors’ calibration method. A robust, fast reconstruction method from multiple RGB-D streams is then proposed, based on an enhanced variation of the volumetric Fourier Transform-based method, parallelized on the GPU, accompanied with an appropriate texture mapping algorithm. On top of that, given the lack of relevant objective evaluation methods, a novel framework is proposed for the quantitative evaluation of real-time 3D reconstruction systems. Finally, a generic, multiple depth streams-based method for accurate real-time human skeleton tracking is proposed. Detailed experimental results with multi-Kinect2 datasets verify the validity of our arguments and the effectiveness of the proposed system and methodologies.

**Index Terms**—3D reconstruction, depth sensors, Kinect, 3D motion capture, skeleton tracking, evaluation, Tele-Immersion

## I. INTRODUCTION

THREE-Dimensional reconstruction of dynamic scenes, including human performers, and human motion tracking are important tasks in the fields of multimedia, computer vision and graphics, with numerous applications, such as human motion analysis and recognition, dynamic 4D media exploration (e.g. in cultural heritage), mixed-reality and 3D Tele-presence / Tele-Immersion. Tele-Immersion (TI) [1] refers to an emerging technology that can support realistic interpersonal communications, allowing geographically distributed users to share an activity in a common virtual space, where users are “immersed” via their real-time 3D “replicant” reconstructions.

Recent technological developments in the fields of real-time 3D capturing (e.g. Kinect, Tango), 3D displays and wearable 3D glasses (e.g. Oculus Rift, Microsoft Hololens), in combination with novel approaches for 4D (3D+time) content production, provide means to support novel applications, such as the above-mentioned ones. For example, recent advances in real-time capturing, full-3D reconstruction and its compression [2] for transmission offer a technological basis to unlock novel 3D tele-immersive pathways.

The authors are with the Information Technologies Institute, Centre for Research and Technology - Hellas, 6th km Charilaou - Thermi, GR-57001, Thessaloniki, Greece, Tel. +30 2310 464160, (e-mail: dalexiad@iti.gr; tofis@iti.gr; nzioulis@iti.gr; ozoidi@iti.gr; glouzis@iti.gr; zarpalas@iti.gr; daras@iti.gr)

Copyright (c) 2016 IEEE. Personal use of this material is permitted. However, permission to use this material for any other purposes must be obtained from the IEEE by sending an email to [pubs-permissions@ieee.org](mailto:pubs-permissions@ieee.org).

This paper describes the main elements of an integrated platform, including capturing and fast 3D reconstruction of human 3D shape/appearance and skeleton-based motion tracking, which targets TI and future 3D applications. The elements of the continuously being developed platform has already allowed the realization of a number of relevant applications, as in <http://vcl.iti.gr/3dTI/>, i) ski competition among users spread around Europe [3], ii) 3D hang-out communications [4], iii) multi-player networked 3D games (“SpaceWars” and “Castle in the Forest”), where users participate via their on-the-fly reconstructed 3D “replicants”, and iv) athletes’ training via professionals’ performance capturing and reconstruction for “quick-post” 4D media. Additionally, the paper describes a novel framework for the objective evaluation of the 3D reconstruction process, where the 3D ground-truth model is not available, as in real-time reconstruction applications.

The paper is organized as follows. In subsection I-A relevant existing work is given, prior to a summary of our contributions in subsection I-B. Section II describes the employed multi-sensor 3D acquisition platform, its synchronization strategy and a novel external calibration method. Sections III and IV provide the details of the proposed methods for 3D reconstruction and skeleton-based human motion tracking, respectively. The experimental results are presented in section V, while conclusions and future work are finally given in section VI.

## A. Previous relevant work

1) *3D capturing and reconstruction*: Several passive RGB cameras-based reconstruction methods can be found in the literature [5], [6], [7]. With the exception of mainly Shape-from-Silhouette (visual-hull) methods [5], which however lack the ability to reconstruct concavities and require a large number of cameras, unfortunately most methods are not applicable in our targeted real-time applications, due to their slow performance. Other, sophisticated human template-based reconstruction (“performance capture”) methods [8], [9], [10] are capable to generate temporally-coherent 3D meshes using less cameras, but still require a processing time of several minutes per frame.

Regarding methods that use active direct-ranging sensors, explicit fusion [11] or volumetric implicit fusion methods [12] until recently had been applied only off-line to combine range data from a single sensor. With the appearance of consumer-grade RGB-D cameras, variations of the referenced approaches have been employed for real-time Tele-presence applications, e.g. [13], [14], [15]. In the category of volumetric reconstruction methods, the Poisson [16] and its ancestor Fourier Trans-

form (FT)-based reconstruction method [17], which require as input an oriented point-set, are worth mentioning, due to their robustness against noise in the input point-normal data. These methods, although fast, cannot perform in real-time.

Real-time, full 3D (i.e. full-body and 360°) reconstruction in this paper is achieved by capturing with multiple RGB-Depth (RGB-D) sensors. An efficient multi-sensor Tele-presence/TI framework has been described in [18], [19], which however compared to our approach (that reconstructs a single 360° full-3D mesh), combines multiple RGB-D data only at the rendering stage to produce intermediate views, in a multi-view depth image-based rendering framework. A single 3D mesh is reconstructed in [15] using a Signed-Distance-based volumetric method [12]. A similar reconstruction approach is described in [14]. Our proposed platform utilizes a volumetric approach, an enhanced variation of the FT-reconstruction method [17], which is parallelized on the GPU to achieve real-time reconstruction rates. Finally, the very recent and promising “Dynamic Fusion” work [20] has to be mentioned, which constitutes an extension of the known “Kinect Fusion” system [21] and can reconstruct slowly deforming objects in a real-time SLAM framework. Nevertheless, it has been applied with a single hand-held RGB-D sensor at close distances and does not address the texture mapping problem.

Although the 3D processing methods, proposed in this paper, apply also with Kinect v1 data, the increased quality offered by the new Kinect generation v2 [22] naturally led to its adoption in our platform, which currently supports both versions. A few works, regarding capturing with multiple Kinects v2, can be found in the literature [23], [24]. In a work [23] slightly relevant to ours, Kinects are used to capture a static room-sized scene into a virtual 3D model, for safe testing of robot control programs. In that paper however, neither the automatic calibration of the sensors, nor the real-time capturing and reconstruction of dynamic scenes is addressed. In a very recent, more relevant work [24], a multi-Kinect2 capturing platform and its calibration are described. A server-client distributed capturing system is proposed, where the clients capture and on-the-fly generate and filter the raw 3D point-clouds, which are either locally stored or transmitted to server, uncompressed in both cases. The software of a similar system can be found in the Brekel toolset (<http://brekel.com/multikinectv2/>). In contrast, in our system, the multiple Kinect RGB-D data are compressed (before locally stored or on-the-fly transmitted) increasing the data rates, and more importantly the data are fused to generate a single, watertight and manifold textured mesh.

**2) 3D reconstruction evaluation:** Early studies on 3D reconstruction systems focused on reconstructing the surface of static objects, in which case the availability of the ground-truth 3D model is possible. Consequently, the reconstruction evaluation can be performed based on a 3D closest-points framework or 3D Hausdorff distance, comparing against the ground-truth model. However, recent 3D reconstruction systems perform fast 3D reconstruction of dynamic scenes captured from a single or from multiple RGB-D cameras [13], [15]. In such a case, the ground-truth model is not available and the reconstruction evaluation is performed mainly subjectively. In this paper, we

propose the first, to the best of our knowledge, framework for objective evaluation of real-time 3D reconstruction systems.

**3) 3D motion capturing:** The most accurate solutions for human motion tracking are marker-based ones, which however are intrusive and require special and expensive equipment, making them prohibitive in many practical applications. Marker-less solutions using a depth sensor are mainly based on human motion databases and machine learning algorithms, enabling reliable human motion tracking by constraining the body configuration space [25], [26]. Kinect user-tracking is based on [26], but due to the one-side field-of-view, it is often problematic in challenging cases, due to self-occlusions.

On the other hand, the proposed platform offers a generic method for accurate, real-time skeleton extraction based on a volumetric human representation (fully exploiting the information offered from the 3D reconstruction), thus overriding the problems in self-occlusion cases. Relevant approaches that try to extract the skeleton from volume data, use mainly multiple RGB cameras and Shape-from-Silhouette (SfS) algorithms [27]. Nevertheless, such approaches require robust silhouette extraction, which is not always an easy task, especially when the background is not static and uniform, introducing errors in the motion capturing method. Another similar method is proposed in [28], where the normalized gradient vector flow is extracted, based on partial differential equations. Likewise, in [29] Laplacian contraction is applied to skeletonize the volume. Although both methods offer a reliable skeleton, the identification and position estimation of the joints are not addressed, while the latter is prohibitive for real-time applications. Finally, Straka *et al* in [30] utilize again a SfS algorithm and, similarly to the proposed method, uses graph-based techniques to detect and extract skeleton in real-time. However, the experimental results provide only a coarse view of the method’s accuracy. In particular, the experimental results present the success-rate in joint position estimation, where as “successful” estimation is defined the case in which the extracted position is within a 100mm radius from the ground-truth. Contrary to that, the reliability and accuracy of our method are demonstrated by comparing the anthropometric angle of the knee and elbow joints (flexion/extension) with state-of-art marker-based motion capturing systems, in challenging performances of Traditional sport “skills”.

### B. Summary of contributions

The major contributions of this paper are listed below:

- A multi-Kinect2 system, with distributed capturing and centralized processing nature. To the authors’ best knowledge, this is among the first works in the literature regarding capturing with multiple Kinect sensors of version 2.
- A novel and fast sensors’ calibration method.
- A real-time reconstruction method from multiple RGB-D streams, which includes an enhanced variation of the volumetric FT-reconstruction method [17], parallelized on the GPU and accompanied with appropriate texture mapping.
- A novel framework for the quantitative evaluation of real-time 3D reconstruction systems from multiple RGB-D streams. To the authors’ knowledge, this is the first work in the literature towards the specific objective.

- A generic method for robust real-time skeleton extraction and tracking from multiple depth streams.
- Finally, a large dataset of multiple synchronized and calibrated RGB-D streams, captured with the proposed system and offered to the research community for experimentation.

## II. CAPTURING SETUP AND CALIBRATION

Although the proposed external calibration and 3D processing methods apply well also with Kinect v1, in this section we focus to the proposed multi-Kinect2 setup.

### A. Capturing system

The proposed system theoretically supports an arbitrary number of sensors, practically limited by the system's complexity, the needed processing power and the local network bandwidth. Additionally, one has to take into account that interference between multiple Kinect v2 sensors exists, although it is less evident and its nature is completely different to that with Kinect v1. For a detailed analysis, the reader is referred to [31]. The devices are placed on a circle of radius  $r \in [2m, 4m]$ , all pointing to the center of the captured area (see also Fig. 2). As a good compromise between system's complexity and coverage area, the use of  $K = 4$  Kinect sensors is proposed. With careful placement of the devices, no major interference issues are observed.

Since Kinect2 limits its usage to one sensor per computer, a network architecture is mandatory. Specifically, the system uses  $K$  computers, where  $K - 1$  of them serve as slave nodes and the remaining one serves as both slave and master node. The captured data arrive at the master node, where processing takes place. The platform operates in two different modes, a **real-time** mode and a **quick-post** one. The first mode continually polls the slave nodes/sensors for new synchronized (up to half of the sensors' internal clock interval) captured data. The latter mode signals all connected nodes to start recording data and finally triggers a "gathering" operation, having all nodes transfer recorded data to the master node. To enable fast transmission in the real-time mode and efficient storage in the quick-post one, an intra-frame compression scheme (JPEG for the RGB and LZ4 entropy compression for the depth images) was employed, due to its reduced complexity and processing time. These modes enable either i) on-line 3D reconstruction, thus making it suitable for TI applications when combined with real-time efficient data compression [2], or ii) temporally-complete and higher quality results, exploiting all the recorded data in a quick-post processing step.

### B. Calibration

**1) Internal calibration:** The Kinect2 depth-to-color mapping operation cannot be expressed as a fixed table, since it depends on the depth measurements. Due to the centralized nature of processing the data, such a mapping table should be transferred to the master node in each frame, which is highly inefficient. Therefore, the mapping is approximated by a fixed KRT matrix (intrinsics and relative pose of the RGB camera). The approximation is performed based on 3D-to-2D correspondences in a dense 3D grid, obtained by employing the Kinect2 SDK functionality.

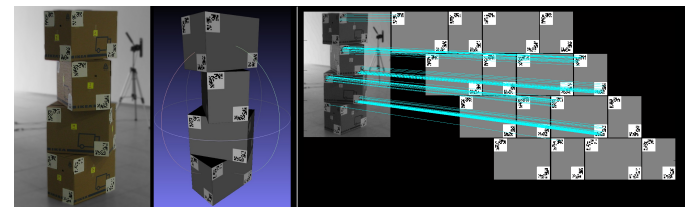


Fig. 1: From left-to-right: (i) The calibration structure, constructed using 4 standardized IKEA boxes (JÄTTENE, 600.471.51), along with 32 unique QR markers [ISO/IEC 18004:2006]; (ii) its digitized 3D counterpart; (iii) the unwrapped texture image  $M(\mathbf{u})$  and SIFT correspondences.

**2) External calibration:** Spatial (external) calibration of the sensors is achieved through a novel registration method, utilizing an easy-to-build calibration structure that serves as a registration "anchor". The registration is performed separately for each sensor, with respect to that "anchor", using an exact digital replica of the calibration object. The approach is based on the Scale Invariant Feature Transform (SIFT) [32] and Procrustes Analysis [33]. Apart from constructing the calibration structure once, no user intervention is needed, in contrast to commonly used methods that require capturing of a moving target.

**Calibration object:** The design of the calibration object was dictated by the following requirements: a) to be universally easily reproducible; b) to exhibit unique texture patterns to support SIFT feature extraction and matching; c) to be sufficiently large, so that estimation/optimization is not affected by noise/inaccuracies in feature extraction and matching. To address these requirements, the calibration structure is realized with 4 standardized IKEA package boxes, of size  $56 \times 33 \times 41$  cm<sup>3</sup>, as well as 32 unique Quick Response (QR) markers of area  $13 \times 13$  cm<sup>2</sup>, placed at the corners of the boxes' side faces. An illustration of the calibration structure is given in Fig. 1(left). As shown, the exact virtual counterpart of the calibration structure, a CAD 3D model, was also designed. A complete manual with instructions and the CAD 3D model can be downloaded from <http://vcl.iti.gr/3dTI/TCSVT>. The virtual model's texture is unwrapped into a single image  $M(\mathbf{u})$ . Let  $\mathcal{V}_M$  denote the set of model's vertices and  $\mathcal{S}_M$  the corresponding texture coordinates in  $M(\mathbf{u})$ .

**Calibration procedure:** The calibration structure is positioned at approximately the center of the capturing space, so that a) the full object is in the field-of-view of all sensors and b) in the case of Kinect v1, to eliminate any bias, as in this case the noise increases with the measured surface's distance.

A color image  $I_k(\mathbf{u})$  and an "accumulated" depth image  $\hat{D}_k(\mathbf{u})$  are acquired for each view-point  $k$ . During this step, to avoid any potential multi-Kinect interference issues, the sensors do not operate concurrently, given that the calibration object is static. The accumulated depth image is obtained as the pixel-wise median, to remove outliers and reduce noise.

SIFT features are extracted from each color image  $I_k(\mathbf{u})$  and feature correspondences are established with the a-priori calculated features of the model texture image  $M(\mathbf{u})$ . Let  $\mathbf{p}_k^j \leftrightarrow \mathbf{p}_M^j, j = 1, \dots, J$  denote the  $j$ -th established correspon-

dence between the feature vector  $\mathbf{p}_k^j$  from image  $I_k(\mathbf{u})$  and the corresponding vector  $\mathbf{p}_M^j$  from  $M(\mathbf{u})$ . Let also  $\mathbf{u}_k^j$  and  $\mathbf{u}_M^j$  denote the corresponding 2D image coordinates of the matched features. Given the  $k$ -th sensor's intrinsic parameters and the depth image  $\hat{D}_k(\mathbf{u})$ , the 2D points  $\mathbf{u}_k^j$  are back-projected to obtain the 3D points  $\mathbf{V}_k^j$ . The unwrapped texture coordinates  $\mathbf{u}_M^j$  are transformed to the 3D vertices  $\mathbf{V}_M^j$  by finding their nearest neighbors in  $S_M$ , and thus, their corresponding vertex position in  $V_M$ . Given the 3D correspondences  $\mathbf{V}_k^j \leftrightarrow \mathbf{V}_M^j$ , the partial Procrustes problem [33] (no scaling and reflection) is solved to estimate the 6DOF pose matrix of the  $k$ -th sensor, i.e. by minimizing the sum of squared distances  $\sum_j \|(\mathbf{R}_k \mathbf{V}_k^j + \mathbf{t}_k) - \mathbf{V}_M^j\|^2$ , subject to  $\mathbf{R}_k^T \mathbf{R}_k = \mathbb{I}_{3 \times 3}$ .

### C. Quick-post synchronization

In order to synchronize the data recorded during the quick-post operation mode, a post-synchronization procedure is employed. Each sensor continuously acquires pairs of timestamped depth and color images. While it is not the exact case, the depth and color components are considered to be synchronized (in practice they are synchronized up to 16msec) and therefore the depth timestamps are used. Each Kinect generates timestamps according to its local time-line  $\mathbb{T}_k$ . An audio synchronization scheme is used to place the local timelines onto a global one. Audio signals of specific duration are simultaneously recorded from each sensor. Let the audio signal from the  $k$ -th Kinect be denoted as  $\mathbf{A}_k(t)$ . Its delay with respect to the reference Kinect  $k_0$  is calculated by  $\hat{d}_k = \arg \max(R_{k,k_0}(d))$ , where  $R_{k,k_0}(d)$  is the cross correlation of audio signals  $\mathbf{A}_k(t)$  and  $\mathbf{A}_{k_0}(t)$ . From these delays, the audio timestamp offsets  $T_k$  are obtained, which are used to place the local time-lines  $\mathbb{T}_k$  onto the reference one  $\mathbb{T}$ .

Let now the RGB-D timestamps, synchronized to the global time-line, be denoted as  $T_k(n), n = 1, \dots, N_k$ , where  $N_k$  is the total number of frames in the  $k$ -th sequence. Under nominal Kinect operation conditions, these timestamps are approximately uniformly spaced, with a time step of 33ms. In practice however, it is observed that frame generation rate can fluctuate. Therefore, a “local synchronization” scheme is employed, which continuously selects new groups of RGB-D frames as follows. Let an RGB-D frame, with timestamp  $T_k(n)$ , be denoted as  $\mathbb{F}_k(n)$ . A synchronized Group-of-Frames (GoF), at a time instance  $m$ , is denoted as  $\mathbb{G}(m) = \{\mathbb{F}_1(n_1(m)), \mathbb{F}_2(n_2(m)), \dots, \mathbb{F}_K(n_K(m))\}$ . The “synchronization inconsistency” of a GoF is measured by the maximum timestamp difference of its frames, i.e.  $\max_{i,j} \{|T_i(n_i(m)) - T_j(n_j(m))|\}$ . Given a GoF  $\mathbb{G}(m)$ , in order to generate the next group  $\mathbb{G}(m+1)$ , all candidate combinations  $\tilde{\mathbb{G}}(m; s) = \{\mathbb{F}_1(n_1(m) + s_1), \mathbb{F}_2(n_2(m) + s_2), \dots, \mathbb{F}_K(n_K(m) + s_K)\}$ , are considered, where  $s = [s_1, s_2, \dots, s_K] \in \{0, 1\}^K$  is a binary string of length  $K$  (excluding zero). Put simply, a new GoF is generated by moving in some or in all the timelines by one step. Among all candidates  $\tilde{\mathbb{G}}(m; s)$ , the one that minimizes the “synchronization inconsistency” is selected. The algorithm continues iteratively, until the end of a sequence.

## III. RECONSTRUCTION OF GEOMETRY AND APPEARANCE

The “performance” of a captured user along time is reconstructed by the extraction of the user's 3D geometry and appearance on a per-frame basis, i.e. for each time instance. Therefore, given multiple captured depth-maps  $D_k(\mathbf{u}), \mathbf{u} = (u, v)^T, k = 1, \dots, K$  at a specific time instance, along with the corresponding RGB images, the objective is the fast 3D reconstruction in the form of a single textured triangular mesh.

Let  $\mathbf{u} \leftarrow \Pi_k(\mathbf{X})$  define the world-to-projective mapping operation, which maps a 3D point  $\mathbf{X} = (X, Y, Z)^T$  to a pixel  $\mathbf{u}$ , while  $\mathbf{X} \leftarrow \Pi_k^{-1}(\mathbf{u}, Z)$  denotes the inverse (projective-to-world) mapping. Similarly, let  $\Pi_k^{\text{RGB}}(\mathbf{X})$  stand for the corresponding mapping for the  $k$ -th RGB camera.

### A. Raw reconstruction and confidence weights

For each “foreground” pixel  $\mathbf{u} \in \mathcal{F}_k$  on the  $k$ -th depth-map, a “raw” 3D point  $\mathbf{X}_k(\mathbf{u}) = \Pi_k^{-1}(\mathbf{u}, D_k(\mathbf{u}))$  is reconstructed. We use the notation  $\mathbf{X}(\mathbf{u})$  to highlight that each reconstructed 3D point  $\mathbf{X}$  is associated with a foreground pixel  $\mathbf{u} \in \mathcal{F}_k$  on the image plane. Additionally, the corresponding “raw” 3D normals  $\mathbf{N}_k(\mathbf{u})$  are estimated as follows: Terrain Step Discontinuity Constraint Triangulation (SDCT) [13] is used to realize an organized triangulation scheme, where each vertex may be connected to one of its eight neighbors (on the 2D image plane). Given the triangle normals, each vertex is assigned the mean of the normals of the triangles into which it participates.

Apart from the raw position-normal information, a confidence-weight map  $W_k(\mathbf{u})$  is calculated on a per-vertex basis, based on the following intuitive observations. The “quality” of a raw measurement depends on the depth-camera's “viewing” angle, i.e. the angle between the camera's line-of-sight and the surface normal. Therefore, a confidence value for a pixel (vertex)  $\mathbf{u} \in \mathcal{F}_k$  is computed from  $W_{k,1}(\mathbf{u}) = \max\{\langle \hat{\mathbf{X}}_k^{\text{loc}}(\mathbf{u}), \mathbf{N}_k^{\text{loc}}(\mathbf{u}) \rangle, 0\}$ , where  $\hat{\mathbf{X}} = -\mathbf{X}/\|\mathbf{X}\|$ ,  $\langle \cdot, \cdot \rangle$  denotes the inner vector product and the superscript “loc” denotes that the 3D positions and normals are defined with respect to the local camera's coordinate system. Additionally, in practice, the depth measurements near the foreground object's silhouette boundaries are noisy. An associated confidence map  $W_{k,2}(\mathbf{u}) \in [0, 1]$  is extracted based on this observation. A fast approach to calculate such a confidence value for a specific pixel  $\mathbf{u}$  is to count the number of foreground pixels inside a square neighborhood around  $\mathbf{u}$ , divided by the neighborhood's size. This is implemented efficiently using a 2D moving average filter (with radius 10pixels in our experiments) on the corresponding binary silhouette image. The final confidence map is calculated from the product  $W_k(\mathbf{u}) = W_{k,1}(\mathbf{u}) \cdot W_{k,2}(\mathbf{u})$ .

### B. 3D volume reconstruction

The objective is to calculate a scalar volume function  $A(\mathbf{q})$ , which implicitly contains the surface information as the isosurface at an appropriate level  $L$ . The function is defined over a 3D grid  $\mathbf{q} = [q_X, q_Y, q_Z]^T \in \{0, \dots, N_X-1\} \times \{0, \dots, N_Y-1\} \times \{0, \dots, N_Z-1\}$ , inside the foreground object's bounding box. To this end, a FT-based approach [17] is employed, enriched with a smoothing and weighting scheme.

The raw normals  $\mathbf{N}_k(\mathbf{u})$  are initially “splatted” to the voxel grid, in order to obtain the gradient vector field  $\mathbf{V}(\mathbf{q})$ . In the simplest, non-weighted version of the method, each raw sample is “clapped” to its nearest voxel, and then the vector field is normalized by the number of samples clapped at each voxel. In the proposed method’s version, the normal  $\mathbf{N}_k(\mathbf{u})$  is smoothly distributed to point’s neighbor voxels, according to:

$$\mathbf{V}(\mathbf{q}) = \sum_k \sum_{\mathbf{u} \in \mathcal{F}_k} g(\mathbf{X}_k(\mathbf{u}), \mathbf{q}; \sigma_1) \cdot [w_k(\mathbf{u}, \mathbf{q}) \cdot \mathbf{N}_k(\mathbf{u})], \quad (1)$$

where  $g(\mathbf{X}_k(\mathbf{u}), \mathbf{q}; \sigma_1)$  are “splatting” weights based on the distance  $x$  of point  $\mathbf{X}$  from voxel  $\mathbf{q}$  and more specifically,  $g(x; \sigma_1) = \sigma_1^{-1} \exp(-x^2/\sigma_1^2)$  is a Gaussian. The confidence-related weights  $w_k(\mathbf{u}, \mathbf{q})$  are obtained from:  $w_k(\mathbf{u}, \mathbf{q}) = W_k(\mathbf{u})/d(\mathbf{q})$ , with the normalization factor  $d(\mathbf{q})$  being a weighted estimate of the points density at the voxel  $\mathbf{q}$ , namely:

$$d(\mathbf{q}) = \sum_k \sum_{\mathbf{u} \in \mathcal{F}_k} g(\mathbf{X}_k(\mathbf{u}), \mathbf{q}; \sigma_2) \cdot W_k(\mathbf{u}), \quad (2)$$

where  $g(x; \sigma_2)$  is again a Gaussian with standard deviation  $\sigma_2$ . In other words, we employ kernel density estimation [34] (taking into account the weights  $W_k(\mathbf{u})$ ), using a Gaussian kernel. In order to avoid singularities,  $\sigma_2$  should always be larger than  $\sigma_1$ . It was experimentally selected equal to  $\sigma_2^2 = \frac{3}{2}\sigma_1^2$ . With respect to  $\sigma_1$ , the larger its value, the smoother the output gradient-field and the reconstruction is expected to be. A reasonable selection is to use a  $\sigma_1$  value that is proportional to the voxel’s diagonal. In our experiments we use a relatively small value, equal to voxel’s radius (half of the diagonal). Given this selection, in order to speed up calculation in our implementation, we consider only the  $4^3$  voxels around each input point, since the values at other voxels will be very low.

Intuitively, the use of the “splatting” weights in (1) is similar (not equivalent) to convolving with a low-pass filter, resulting into a smooth gradient field. The use of the density-normalized weights  $w_k(\mathbf{u}, \mathbf{q})$  assigns smaller weights to non-confident input samples at high-density regions, letting other confident points in the neighborhood to contribute more in the reconstruction of the gradient field.

Subsequently, following [17], the calculated gradient field  $\mathbf{V}(\mathbf{q}) = [V_X(\mathbf{q}), V_Y(\mathbf{q}), V_Z(\mathbf{q})]^T$  is transformed into the 3D frequency domain, by applying 3D FFT separately to each of vector field’s  $X$ ,  $Y$ ,  $Z$  components, to obtain  $\hat{\mathbf{V}}(\omega) = [\hat{V}_X(\omega), \hat{V}_Y(\omega), \hat{V}_Z(\omega)]^T$ , where  $\omega = (\omega_x, \omega_y, \omega_z)^T$  is the 3D frequency vector. The integration filter  $\hat{\mathbf{F}}(\omega) = [\hat{F}_X(\omega), \hat{F}_Y(\omega), \hat{F}_Z(\omega)]^T = \frac{1}{\|\omega\|^2} [j\omega_x, j\omega_y, j\omega_z]^T$ ,  $j = \sqrt{-1}$ , is applied by multiplication in the frequency domain.

The final volumetric function  $A(\mathbf{q})$  is calculated by applying the inverse 3D FFT on the integrated (filtered) vector field and adding its  $X$ ,  $Y$ ,  $Z$  components. The purpose of applying the integration filter in the frequency domain is justified by the IIR (Infinite Impulse Response) nature of the filter, which does not allow for parallel calculations on the GPU if applied in the original domain, as well as by the existence of very fast FFT implementations.

It has to be recalled here that multiplication in the discrete Fourier domain is equivalent to circular convolution in the original spatial domain. Therefore, to avoid any unwanted

effects of circular convolution, the tight foreground object’s bounding box is adequately extended before voxelization (equivalent to zero padding of  $\mathbf{V}(\mathbf{q})$ ).

The final 3D surface is extracted in the form of a triangle mesh (vertex positions, normals and connectivity), as the isosurface  $A(\mathbf{q}) = L$  using the marching cubes algorithm [35]. The level  $L$  is calculated as the average value of  $A(\mathbf{q})$  at the input sample locations  $\mathbf{X}_k(\mathbf{u})$ . The whole reconstruction method was implemented with CUDA ([www.nvidia.com/object/cuda\\_home\\_new.html](http://www.nvidia.com/object/cuda_home_new.html)) for parallel computing on the GPU, since most of its stages involve pixel- or voxel-wise calculations.

### C. Texture mapping - Reconstruction of appearance

Many vertices in the final reconstructed model are visible in more than one RGB cameras. Therefore, colors from more than one RGB camera have to be combined to produce the color of each reconstructed vertex. There are two important issues that need to be taken into account and can significantly improve the visual quality of the rendered reconstruction. Firstly, volumetric 3D reconstruction methods generally produce a relatively low number of triangles and vertices (depending on the volume resolution), lower than the number of pixels in the original 2D domain. Therefore, a color-per-vertex rendering approach will lead to color aliasing, producing low visual quality. Instead, we employ full texture-mapping and assign multiple texture patches to each triangle, from the multiple RGB views. Secondly, instead of using equal weights for each “visible” RGB camera, one could use weights based on the “quality” of the captured colors. Practically, given that the RGB cameras are more-or-less equidistant from the captured user, a) the quality of the “captured” color depends on the “viewing” angle of the captured surface, i.e. it depends on the angle between the line-of-sight and the surface normal. Additionally, b) near the captured object boundaries, inaccurate Depth-to-RGB camera registration (calibration) may lead to color-mapping artifacts (e.g. color of the background assigned on the reconstructed foreground object). Therefore, the captured color information near the object boundaries have to be assigned a smaller weight. It should be noted now that the depth image-based weights  $W_k(\mathbf{u})$  in subsection III-A were defined based on similar intuitions. Finally, given that the depth and RGB cameras of a single Kinect-like RGB-D device are parallel and very close to each other, it can be practically considered that the visibility of a vertex is the same in both cameras. In practice, this approximation proved to be helpful in speeding-up calculations without introducing significant color artifacts. Since the weights  $W_k(\mathbf{u})$  contain visibility information and incorporate the practical observations for weighting, they are directly used in the texture mapping process.

Formally, let  $\mathcal{V}(\mathbf{X}) \subseteq \{1, \dots, K\}$  denote the subset of depth cameras in which the vertex  $\mathbf{X}$  is visible. Let also  $\mathbf{u}_k, k \in \mathcal{V}(\mathbf{X})$  be the corresponding pixels on the “visible” depth cameras, where the vertex  $\mathbf{X}$  projects according to  $\mathbf{u}_k = \Pi_k(\mathbf{X})$ . Similarly, let  $\mathbf{u}_k^{\text{RGB}} = \Pi_k^{\text{RGB}}(\mathbf{X})$  be the corresponding pixels (UV-coordinates) on the “visible” RGB cameras. Each vertex is assigned multiple weights  $W_k(\mathbf{u})$  and UV texture

coordinates  $\mathbf{u}_k^{\text{RGB}}$  on the corresponding “visible” images. Each reconstructed triangle is rendered with OpenGL multi-texture blending, using the associated vertices’ weights.

### D. Color correction

The RGB cameras of consumer-grade sensors, especially under non-uniform lighting and background conditions, may output color values that vary significantly between adjacent RGB views, i.e. the color of the same 3D point appears different in two captured RGB views. To attenuate the resulting texture artifacts, we search for the color-correction functions that minimize (in a robust mean-square sense) the color difference between pairs of pixels in two cameras that capture (approximately) the same 3D point. Our approach borrows ideas from [18], but uses the HSV colorspace instead.

1) *Searching for color correspondences*: Consider two adjacent RGB cameras, with overlapping field-of-view, indexed with  $k_1$  and  $k_2$ . Let the raw vertex positions for a given frame be denoted as  $\mathbf{X}_{k_1}^i, i = 1, \dots, I$  and  $\mathbf{X}_{k_2}^j, j = 1, \dots, J$ , respectively, whereas the corresponding raw RGB vertex colors be  $\mathbf{C}_{k_1}^i$  and  $\mathbf{C}_{k_2}^j$ . The “mutual” closest points between the point-clouds, with Euclidean distance smaller than 20mm, are searched. This way, a number of color correspondences  $\mathbf{C}_{k_1}^m \leftrightarrow \mathbf{C}_{k_2}^{n(m)}, m = 1, \dots, M$ , is found. To achieve robustness, color correspondences in multiple frames are accumulated.

2) *Estimating color-correction functions*: The objective is to find a linear function  $\mathbf{F}_{k_1, k_2}(\mathbf{C})$  such as  $\|\mathbf{F}_{k_1, k_2}(\mathbf{C}_{k_1}^m) - \mathbf{C}_{k_2}^{n(m)}\|$  is minimized. We found in practice that an RGB-separated approach [18] may be ill-posed when the range of colors in the foreground object is limited, e.g. when a specific color channel is missing. On the other hand, by working in the HSV color-space, it is expected that the Hue component is not affected by the exposure control, while it was experimentally found that the Saturation component is only slightly affected. Therefore, the correspondence colors are transformed into the HSV color-space and a linear mapping model is built by robust (RANSAC) linear regression on the Value data  $V_{k_1}^m$  and  $V_{k_2}^{n(m)}, m = 1, \dots, M$ , such that  $|F_{k_1, k_2}(V_{k_1}^m) - V_{k_2}^{n(m)}|$  is minimized in a (robust) mean-square sense. Given a reference camera, the final color-correction function for a specific camera is obtained by considering the path from that camera to the reference.

### E. Methodology for quantitative objective evaluation

In order to objectively evaluate the performance of a real-time 3D reconstruction method, a capturing system consisting of  $K + K'$  calibrated RGB-D sensors is employed, where  $K$  sensors take part in the reconstruction procedure and  $K'$  sensors serve as additional ground-truth planar views of the user. Such a capturing system is shown in Fig. 2. The proposed objective evaluation framework aims at addressing the following question: How well does the reconstructed mesh “explain” (match) the captured data in all available 2D views? The comparison is performed on the 2D image plane, by i) projecting the reconstructed mesh into the  $K+K'$  planar views and ii) comparing the “rendered” depth and color images (the depth- and color- buffers of the OpenGL frame-buffer) with the original captured views. Since the ground truth data are

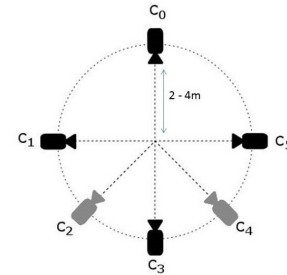


Fig. 2: Camera setup for 3D reconstruction and quantitative evaluation.  $K = 4$  sensors ( $c_0, c_1, c_3$ , and  $c_5$ ) take part in the reconstruction process and  $K' = 2$  sensors ( $c_2, c_4$ ) serve as additional ground-truth views.

sensor data, they may suffer from noise, especially near the border areas between the user and the background. This means that, the employed performance measures may sometimes deteriorate due to bad ground-truth model assumption. Such situations will be further discussed in the experimental section.

1) *Evaluation of the reconstructed volume*: The reconstructed 3D shape may suffer from holes, missing/cut limbs and model distortions. In order to quantify such errors, the percentage of the non-reconstructed object volume is estimated based on the silhouette information, as follows. Firstly, the reconstructed 3D mesh is projected onto the depth image plane of sensor  $c_k, k = 1, \dots, K + K'$  and the reconstruction’s binary 0/1 silhouette mask  $S_k^r$  is extracted. The ground-truth silhouette mask  $S_k^g$  is also extracted by performing foreground-background segmentation on the sensor depth. The “volume reconstruction error” (VRE) metric is calculated from:

$$V_k = |S_k^r \oplus S_k^g| / |S_k^r \vee S_k^g|, \quad (3)$$

where  $\oplus$  and  $\vee$  denote the binary operators XOR and OR, respectively and  $|\cdot|$  is the silhouette mask area. Due to the XOR operation, the metric punishes both false positive and false negative silhouette areas. Another used silhouette-based metric is the 2D Hausdorff distance [36], expressed in pixels:

$$H_k = \max \left\{ \sup_{\mathbf{u}_r \in S_k^r} \inf_{\mathbf{u}_g \in S_k^g} d(\mathbf{u}_r, \mathbf{u}_g), \sup_{\mathbf{u}_g \in S_k^g} \inf_{\mathbf{u}_r \in S_k^r} d(\mathbf{u}_r, \mathbf{u}_g) \right\}, \quad (4)$$

where  $d(\mathbf{u}_r, \mathbf{u}_g)$  denotes the 2D distance between the pixel  $\mathbf{u}_r$  in the reconstructed silhouette mask and the pixel  $\mathbf{u}_g$  in the ground-truth mask. When the reconstructed model contains holes, the Hausdorff distance is equal to the radius of the circle, inscribed to the hole. When it contains a missing or cut limb, the metric will be equal to the length of the that limb.

2) *Evaluation of the reconstructed geometry*: In order to evaluate how accurately the 3D geometry is reconstructed, a 3D closest-point approach is employed. Firstly, the ground-truth foreground depth image of the sensor  $c_k$  is back-projected onto the 3D space to generate a point-cloud  $\{\mathbf{X}_{k,i}^g, i = 1, \dots, I_k\}$ . The point-cloud  $\{\mathbf{X}_{k,j}^r, j = 1, \dots, J_k\}$  is also generated from the corresponding depth image obtained from the reconstructed mesh. The use of a closest-point rooted mean square error (CP-RMSE) metric is proposed, given from:

$$\text{CPRMSE}_k = \sqrt{\frac{1}{I_k} \sum_{i=1}^{I_k} \inf_{j=1, \dots, J_k} \left\{ \|\mathbf{X}_{k,i}^g - \mathbf{X}_{k,j}^r\|^2 \right\}}. \quad (5)$$

A closest-point MSE metric is employed instead of 3D Hausdorff distance between surfaces, since the latter would require connectivity information for the ground-truth point-cloud, and more importantly, due to its sup operation (instead of mean), it would mainly count for missing limbs (as in the previous paragraph), instead of the reconstruction geometry accuracy.

*3) Evaluation of the appearance quality:* The evaluation of the appearance quality is perceived as an image quality assessment task: How well does the ground-truth RGB image, captured from a specific view-point, match the textured model, rendered from exactly the same view-point? Due to the poor performance of MSE and PSNR as visual quality metrics [37], a Structural Similarity Index (SSIM)-based measure [38] was chosen in our framework. The SSIM between two images, evaluated at pixel  $\mathbf{u}$ , is given from:  $\text{SSIM}(\mathbf{u}) = [l(\mathbf{u})]^{\alpha} \cdot [c(\mathbf{u})]^{\beta} \cdot [s(\mathbf{u})]^{\gamma}$ , where  $\alpha, \beta, \gamma$  are constant exponents and

$$l(\mathbf{u}) = \frac{2\mu_X\mu_Y + C_1}{\mu_X^2 + \mu_Y^2 + C_1}, \quad c(\mathbf{u}) = \frac{2\sigma_X\sigma_Y + C_2}{\sigma_X^2 + \sigma_Y^2 + C_2}, \quad s(\mathbf{u}) = \frac{2\sigma_{XY} + C_3}{\sigma_X\sigma_Y + C_3} \quad (6)$$

are the “luminance”, “contrast” and “structural” terms, respectively.  $C_1, C_2, C_3$  are small constants and  $\mu_X, \mu_Y, \sigma_X, \sigma_Y, \sigma_{XY}$  stand for the images’ means, standard deviations and cross-covariances in a neighborhood  $\mathcal{N}(\mathbf{u})$  around pixel  $\mathbf{u}$ . In this work, a variation of SSIM is employed, the Weighted Multi-Scale SSIM (WMS3IM) [39], evaluated at  $J = 3$  scales. WMS3IM is calculated from:  $\text{WMS3IM}_k(\mathbf{u}) = \prod_{j=1}^3 l_j^{\alpha_j} c_j^{\beta_j} s_j^{\gamma_j}$ , where  $j = 1, 2, 3$  stands for the scale and the constants  $\alpha_j, \beta_j, \gamma_j$  have been set based on the psychovisual experiments of [40] and more specifically:  $\{\alpha_1, \alpha_2, \alpha_3\} = \{0, 0, 0.1333\}$  and  $\{\beta_1, \beta_2, \beta_3\} = \{\gamma_1, \gamma_2, \gamma_3\} = \{0.0448, 0.3001, 0.1333\}$ . The “structural” term at scale  $j$  is calculated from:

$$s_j = \frac{\sum_{\mathbf{u} \in S_k^r} s(\mathbf{u}) w(\mathbf{u})}{\sum_{\mathbf{u} \in S_k^r} w(\mathbf{u})}, \quad (7)$$

where the weights in our case are  $w(\mathbf{u}) = \sum_{\mathbf{v} \in \mathcal{N}(\mathbf{u})} S_k^r(\mathbf{v})$ . Similar equations are used to calculate the “luminance” and “contrast” terms  $l_j$  and  $c_j$ .

#### IV. VOLUME-BASED MOTION TRACKING

In this section, a fast method for human skeleton tracking is presented, exploiting the human volume reconstructed as in section III. The method tracks the joint positions of a 15-joints skeletal structure, illustrated in Fig. 3. This structure is separated into a) the rigid-body part that includes the “torso”, “hip”, “neck” and “shoulder” joints, and b) the limb-parts that consist of the “elbow” and “wrist” or the “knee” and “ankle” joints. The rigid-body part is a group that moves rigidly, based on the assumption that the relative rotations of the upper- and lower- body trunk can be ignored. This simplification, although constitutes a limitation, introduces robustness.

The proposed method consists of two phases. Initially, in a “user-calibration” phase, the user body structure is estimated. Then, during the “main tracking” phase, both the position-orientation of the rigid-body part and the limb-joint positions are tracked. The main tracking algorithm is initially described, assuming that the necessary “user-calibration” data are known, before going into the description of the “user-calibration” phase in subsection IV-B. The algorithm steps, performed on a per-frame basis, are given sequentially in the next section.

#### A. Main tracking algorithm

**Volume binarization and skeletonization:** Given the reconstructed volume function  $A(\mathbf{q})$  and the corresponding isosurface level  $L$  (subsection III-B), the binary human volume  $A_h(\mathbf{q}) \in \{0, 1\}$  is extracted (Fig. 4(a)). Skeletonization is then realized (Fig. 4(b)), using the method in [41]. The result is denoted as  $A_s(\mathbf{q})$ . Additionally, we let  $Q_h$  denote the set of voxels belonging to the binary volume  $A_h$ , i.e.  $Q_h = \{\mathbf{q} : A_h(\mathbf{q}) = 1\}$ , and  $Q_s$  the voxels belonging to the skeletonized volume, respectively.

**Estimation of torso position:** Given the structure and symmetry of the human body, the torso is in most cases the joint closest to the human mass center [42]. Therefore, the “most centralized” voxel of  $Q_h$  is initially searched. More specifically, let  $\mathbf{p}(\mathbf{q})$  denote the 3D coordinates of voxel  $\mathbf{q}$ . The average Euclidean distance of a voxel  $\mathbf{q}$  with the rest voxels is  $D(\mathbf{q}) = \frac{1}{|Q_h|} \sum_{\mathbf{q}_i \in Q_h} \|\mathbf{p}(\mathbf{q}_i) - \mathbf{p}(\mathbf{q})\|$ , where  $|Q_h|$  is the cardinality of  $Q_h$ . The point  $\mathbf{p}(\mathbf{q}_c)$  for which  $D(\mathbf{q})$  is minimized, represents the voxel closest to the torso. The point in the set  $Q_s$ , closest to  $\mathbf{p}(\mathbf{q}_c)$ , represents the detected torso position and is notated as  $\mathbf{p}_t$ .

**Detection of extreme joints (head, wrists and ankles):** Towards our objective a graph-based technique is utilized.

*1) Graph and Minimum Spanning Tree (MST):* The points of the skeletonized set  $Q_s$  are considered as the vertices (nodes)  $\mathcal{V}_s$  of a graph  $\mathcal{G}(\mathcal{V}_s, \mathcal{E})$ , where  $\mathcal{E}$  is the edge set. The graph is constructed by connecting the nodes with Euclidean distance lower than a predefined radius (i.e.  $\sim 15\text{cm}$ ), so that only neighboring vertices are connected. The cost of an edge between two connected nodes is set equal to their Euclidean distance. The cost along a path from one node to another equals their geodesic distance. The Minimum Spanning Tree (MST), let  $\mathcal{T}$ , is extracted from  $\mathcal{G}$ , using Kruskal’s algorithm [43], as shown in Fig. 4(c). The MST provides an initial skeleton-like model, with unique paths from node to node.

*2) Extreme joints detection:* Exploiting the structure of the given MST, under normal circumstances, its leaves correspond to the human body extremities, as depicted in Fig. 4(d). These 5 extremities need to be labeled as “ankle”, “wrist” or “head”.

However, in special cases, the leaves of the initial tree  $\mathcal{T}$  may not count to  $N = 5$ . Let  $N_d$  denote the number of the MST’s leaves. In the non-standard case of  $N_d < 5$ , indicating possible body part stacking, a heuristic approach is used: The two “lower” detected leaves (their 3D positions have the lowest values along the Y-axis) are labelled as “ankle” joints. Given that, let  $\mathcal{T}_{\text{low}}$  denote the sub-tree that includes the paths from the ankles to the torso. Subtracting  $\mathcal{T}_{\text{low}}$  from  $\mathcal{T}$  (i.e. dropping the nodes of  $\mathcal{T}_{\text{low}}$  and their incident edges), the upper-body sub-tree  $\mathcal{T}_{\text{up}} = \mathcal{T} \setminus \mathcal{T}_{\text{low}}$  is obtained. In cases of holding the hands stacked on the body, the number of the leaves of  $\mathcal{T}_{\text{up}}$  will be equal to 3, i.e. the “wrists” joints are revealed. In the other non-standard, rare case of  $N_d > 5$ , indicating “spurious artifact limbs”, the detected leaves are filtered based on their geodesic distance to the torso. The paths with geodesic lengths closer to those estimated during the calibration phase are selected, while the rest of them are dropped. Thus, the number of the leaves in the final tree equals to  $N = 5$ .

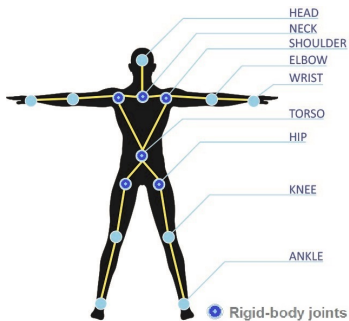


Fig. 3: The 15-joints structure, separated into the rigid-body part and the limbs part.

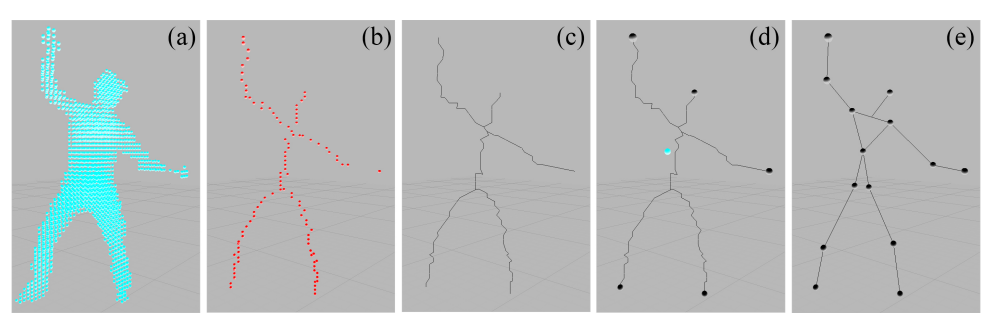


Fig. 4: Overview of the main stages of the proposed method. a) The initial binary volume  $A_h$ , b) the skeletonized volume  $A_s$ , c) the Minimum Spanning Tree (MST) of graph  $G(V_s, E_s)$ , d) the 6 basic/initial joints detection and e) the final extracted skeleton.

Let  $\mathcal{H} = \{H_p\}_{p=1,\dots,10}$  denote the set of all paths from extremity to extremity. Let also  $\mathcal{B} = \{B_p\}_{p=1,\dots,6}$  denote the subset of  $\mathcal{H}$  that includes only the paths passing through the torso point  $p_t$ , i.e. the paths from an upper-body extremity to a lower-body one. The intersection of the paths in  $\mathcal{B}$ , (i.e. keeping only the nodes common in these paths) gives the “spine” path  $S$ . The detection of the spine path is crucial, since its usage is twofold: i) it separates the extremities into the upper-body (“wrists” and “head”) and lower-body (“ankles”) groups. The upper-body joint with the shortest path to the torso is labelled as the “head”; ii) the torso orientation can be estimated by applying PCA on the area around the spine.

**Torso orientation estimation and rigid-body update:** Given the spine path  $S$  and the initial volume  $A_h$ , we extract the points in the area of the thorax, the abdominal and the pelvis segments, by considering a radius  $r$  whose value depends on the human-body volume, around the points of the spine. Let the set of these points be  $P_{tr}$ . By applying PCA to  $P_{tr}$ , the torso orientation  $R_t$  is estimated. Assuming that the neck, the shoulders, the hips and the torso are rigidly connected (rigid-body part), we use  $R_t$  and the torso-position  $p_t$  to transform the root-rigid body in the world space.

**Detection of link joints (elbows and knees):** Let  $\mathbf{X}_r$  and  $\mathbf{X}_x$  stand for the position of the root joint (i.e. hip or shoulder) and the corresponding human extremity (i.e. wrist or ankle) of a limb, respectively. Let also  $\mathbf{X}_j$  be the position of a node along the path from  $\mathbf{X}_r$  to  $\mathbf{X}_x$ . The bone lengths are considered to be known, estimated during the user-calibration phase. The positions of the link joints are extracted from:

$$\hat{\mathbf{p}} = \arg \min_j \left( \left| \| \mathbf{X}_j - \mathbf{X}_r \| - d_r \right| + \left| \| \mathbf{X}_j - \mathbf{X}_x \| - d_x \right| \right), \quad (8)$$

where  $d_r$  is the bone length from joint  $r$  to  $j$  and  $d_x$  the length from joint  $x$  to  $j$ . This means that  $\hat{\mathbf{p}}$  is given as the point on the skeleton graph that intersects with the circular patch obtained from the intersection of the spheres  $\{\mathbf{X}_r, d_r\}$  and  $\{\mathbf{X}_x, d_x\}$ .

**Kalman filtering:** Kalman filtering [44] is applied on a per-joint basis, in order to achieve a smooth transition from frame to frame and avoid errors from volume noise. Erroneous estimates of joint positions (especially under circumstances like self-occlusion or ghost limbs) can be partially corrected by imposing inter-frame correlation of joint positions via Kalman Filtering. In the employed Kalman-filter model, the

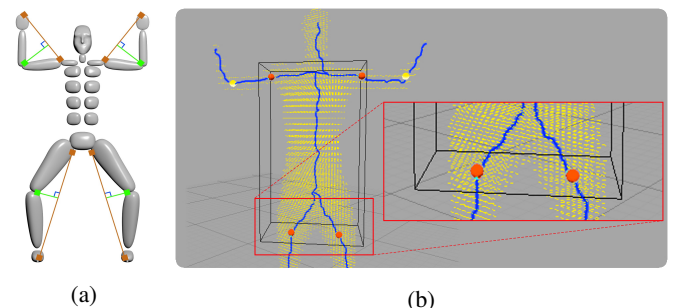


Fig. 5: User calibration in X-pose: (a) Estimation of bone lengths. (b) Extraction of the rigid-body structure.

“state transition” matrix is set based on the Newtonian law  $\mathbf{p}(t) = \mathbf{p}(t-1) + \mathbf{v}(t-1)$ , while the measurement/observation vector corresponds to the estimated 3D joint position and is modelled as the actual position plus zero-mean Gaussian white noise.

### B. Human body structure calibration

The calibration phase assumes that the user is standing in X-pose, shown in Fig. 5(a). Initially, the rigid-body part structure is estimated, as shown in Fig. 5(b). The bounding box of the body trunk is extracted and the intersections of the edges of the MST with this bounding box gives the shoulders and hips joints. The neck is extracted as the midpoint between the shoulders. The positions of the link joints (elbows and knees) in X-pose (Fig. 5(a)) are then extracted from:

$$\hat{\mathbf{p}} = \arg \max_j \left( \frac{\| (\mathbf{X}_j - \mathbf{X}_r) \times (\mathbf{X}_x - \mathbf{X}_r) \|}{\| (\mathbf{X}_x - \mathbf{X}_r) \|} \right). \quad (9)$$

The notation is similar to the one in eq. (8). According to (9), based on human body bones rigidness, the point with the maximum distance from the line segment that connects the joints (e.g. shoulder with wrist) represents the link-joint position, as shown in Fig. 5(a). During the calibration phase, apart from the bone lengths, the geodesic lengths of the paths from each joint to torso are extracted.

The method is applied for a sequence of frames, instead of a single frame. The body structure definition is considered complete after a few frames, in which, rules of human body symmetry and estimation repeatability were satisfied.



Fig. 6: “Argyris” sequence - (a) Initial Kinect data, i.e. four separate meshes [13], vs proposed watertight reconstructed geometry; (b) Results with color - From left to right: (i) Four separate meshes, (ii) Poisson reconstruction [16] (resolution  $2^r \times 2^r \times 2^r$ ) and (iii) proposed watertight volumetric reconstruction (resolution  $2^r \times 2^{r+1} \times 2^r$ ), all with color-per-vertex information without weighted combination of the colors, i.e. equal weights are used; (iv) Using weighted blending of the RGB textures, based on the proposed weights. The texture is sharper and the colors are smoothly blended.



Fig. 7: “Argyris” sequence - For each pair, the proposed watertight reconstruction (right) is compared with TSDF-based reconstruction (left), at the same volume resolution.



Fig. 9: “Stavroula” sequence (Kinect1 data) - From left-to-right: (i) Raw reconstruction (five separate meshes); (ii),(iii) The effect of color-correction: Without and with color correction. In both cases, weighted texture blending was applied.

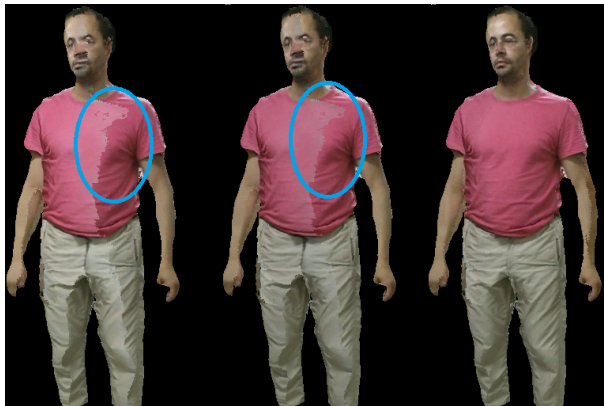


Fig. 8: “Giorgos” sequence - The effect of color-correction and weighted texture blending. From left to right: (i) Initial, (ii) after color correction, (iii) and after weighted blending.

## V. EXPERIMENTAL RESULTS

We initially present results of the employed capturing and reconstruction method, in terms of subjective 3D geometry/appearance reconstruction quality and processing time, before going into an objective quantitative evaluation analysis, which is based on the proposed framework of section III-E. In

subsection V-C, experimental results of the proposed human skeleton tracking method are finally presented.

Additional experimental results, in the spirit of this section, can be found in the supplementary document, along with supplementary videos, at <http://vcl.iti.gr/3dTI/TCSVT>. The datasets used in this section can be downloaded from:

<http://vcl.iti.gr/3dTI/TCSVT/dataset>.

### A. 3D reconstruction results and processing time

Most results were obtained using capturing setups with multiple Kinects2, in both small-area and medium-area spatial configurations. In the second case, professional athletes are captured, performing “skills” of traditional Gaelic and Basque sports. The presented results were obtained using a volume resolution  $2^r \times 2^{r+1} \times 2^r$  with  $r = 7$ , unless otherwise stated. Notice that the resolution along Y is doubled, as the human bounding box is larger along its height.

#### Small-area configuration

Four sensors are placed on a circle of radius approximately 2.5m, with an individual performing athletic movements at the center of the captured space.

1) “Argyris” sequence: In Fig. 6(a), the proposed reconstruction result is compared with the initial reconstructed data (four aligned separate meshes), in terms of 3D geometry.



Fig. 10: Gaelic football “punt kick” - From left to right: (i) Original RGB view, (ii) raw reconstruction (four separate meshes) and (iii) proposed reconstruction from two view points.

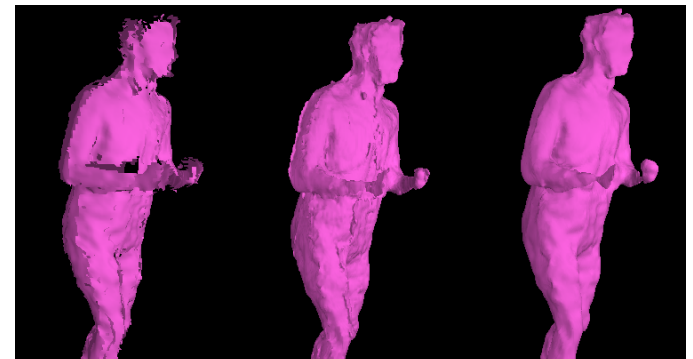


Fig. 11: Gaelic football - From left to right: (i) raw reconstruction; (ii) Reconstruction without and (iii) with the smoothing and confidence-based weighting in equation (1).

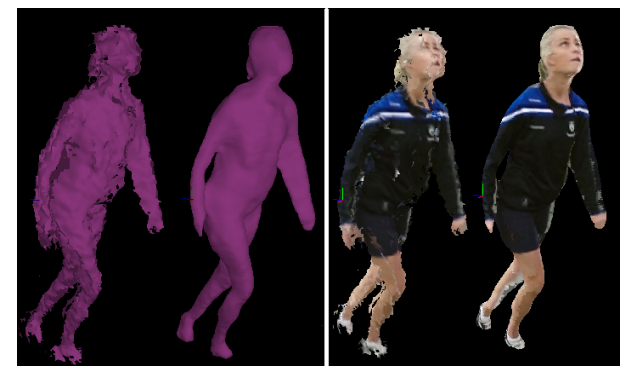


Fig. 12: Gaelic football “Overhead Catch” - Left: Raw reconstruction vs proposed reconstruction (geometry only). Right: Raw reconstruction vs proposed reconstruction, with weighted UV-texture mapping.



Fig. 13: “Jai Alai Backhand Shot” - From left to right: (i) Reconstructed geometry; (ii) original view; (iii) textured mesh, rendered from two view points.



Fig. 14: “Pala Straight-arm Side Shot” - Original view vs rendered reconstruction from two view points - Due to the fast motion under non-perfect synchronization conditions, thin structures like the arms are not well reconstructed.

TABLE I: Comparative results: Average time (msec) of the volumetric methods, for the “Argyris” sequence

Vol. Recon. Method	Reconstruction resolution		
	$r = 5$	$r = 6$	$r = 7$
Vol. FT-based proposed (simple)	10 msec	22 msec	102 msec
Vol. FT-based proposed	17 msec	27 msec	163 msec
Vol. Poisson [16]	385 msec	1061 msec	4602 msec
Vol. TSDF-based [12], [21]	10 msec	21 msec	89 msec

TABLE II: Average reconstruction time (msec) and rates for “Argyris” sequence

Method’s step	Reconstruction resolution		
	$r = 5$	$r = 6$	$r = 7$
Raw point-normal reconstruction		15 msec	
Calcul. of confidence weights		4 msec	
Vol. FT-based proposed (simple)	10 msec	22 msec	102 msec
Other (e.g. texture mapping)	5 msec	23 msec	46 msec
Total (msec)	34 msec	64 msec	167 msec
Rate (fps)	29.4 fps	15.6 fps	6.0 fps

notice in Fig. 9(left) the noisy nature of the input Kinect1 data, due to multi-Kinect interference.

#### Medium-area configuration: Traditional sport “skills”

The reconstruction of traditional sport performances is considered in the current subsection. The capturing setup consists of four Kinect2 sensors, placed on a circle of radius close to 4m. The athletes perform fast sport “skills”, within a large area, sometimes at the distance limits of Kinect2.

4) *Gaelic football “Punt kick”*: Figure 10 depicts an example 3D reconstruction of an athlete during the execution of a Gaelic football “skill”. Due to the lack of perfect synchronization and the relatively fast motion (notice that the motion blur is visible even in the original view), the captured data are not perfectly aligned. However, the method reconstructs a good-shaped model, while the texture weighting method reduces the artifacts significantly.

Figure 11 demonstrates the positive effect of the smoothing and confidence-based weighting in equation (1), especially at the separate meshes’ boundaries, where noisy input point positions and normals may introduce artifacts.

5) *Gaelic football “Overhead catch”*: The reconstructed 3D geometry of the proposed method is compared to the originally captured data (four separate meshes) at the left Fig. 12. The volume resolution here is  $2^r \times 2^{r+1} \times 2^r$  with  $r = 6$ . As can be seen, due to the low resolution of the voxel grid, some details, e.g. the hands, are lost. Additional reasons are i) the low density of the input captured 3D points (the athlete is far from the cameras); ii) the non perfect synchronization, which causes data to be not perfectly aligned and opposite surfaces to “cancel out” each other.

At the right of Fig. 12, the corresponding final UV-textured model is depicted versus the originally captured data.

6) *Traditional Basque sports*: In Fig. 13 an athlete is reconstructed performing a traditional Basque sport “skill”. Despite the large capture distance and the relatively fast motion, the 3D reconstruction method “captures” acceptably well the shape and appearance of the athlete.

An additional example is given in Fig. 14, with a female athlete in a fast “skill”. In this case, thin structures, such as the arms, are not well reconstructed, due to very fast motion under

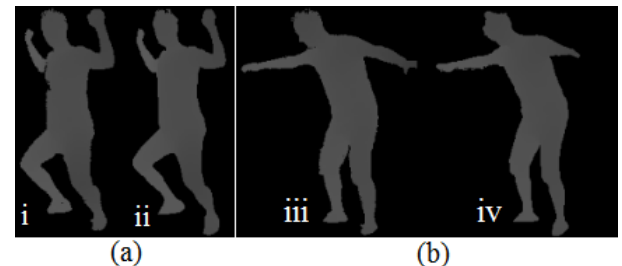


Fig. 15: For each pair: (i),(iii) Originally captured depth, serving as ground truth, and (ii),(iv) the reconstructed one.

non-perfect synchronization conditions. This example reveals the limitation of the capturing system in very fast movements, as any multi-camera system without external hardware-based triggering synchronization. This limitation dictates directions for our future work, as will be discussed in section VI.

#### Reconstruction Time / Rate

The proposed GPU volumetric reconstruction was applied for voxel-grid resolutions  $2^r \times 2^{r+1} \times 2^r$ , with  $r = 5, 6$ , and 7. Similarly, a TSDF-based reconstruction was employed, using the optimized GPU implementation of the Point-Cloud library (ver.1.8.0, <http://pointclouds.org/>). Finally, the Poisson reconstruction method [16] was applied with a tree-depth equal to  $r + 1$ , which corresponds to the same voxel-grid resolution, halved along Y. The average number of vertices produced by the proposed method at  $r = 7$  is 90K vertices, whereas the corresponding number for Poisson reconstruction is approximately the half.

Table I provides mean execution time results for the proposed volumetric FT-based reconstruction method vs the Poisson method and the TSDF method, considering the “Argyris” sequence. The experiments ran on a PC with an i7 processor (3.2GHz), 8GB RAM and a CUDA-enabled NVidia GTX 560. As shown in the third row of Table I, the mean reconstruction time for the CPU Poisson method is above 4sec at  $r = 7$ , whereas the GPU implemented (weighted) FT-based method requires 163msec, as given in the third row. The corresponding number for the simple version of the method (without the weighting scheme in equation (1)), is 102msec. Therefore, for TI applications in the real-time mode, the simple reconstruction version is used, to increase the reconstruction rate. Compared to the optimized GPU TSDF reconstruction, the proposed method can run at similar time, while producing superior results, as shown in Fig. 7.

Considering all the steps of the reconstruction framework, given in Table II, the total reconstruction time is 167msec at  $r = 7$ , which results into near real-time frame rates. The corresponding number for  $r = 6$  is 64msec (15.6 fps), which is quite satisfactory for TI applications with consumer-grade equipment.

#### B. 3D reconstruction - Quantitative evaluation

The experimental results presented here were extracted from the “Argyris” sequence. Additional results are given in the supplementary document. The objective is threefold: a) to highlight some practical limitations of the quantitative

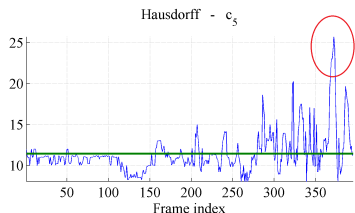


Fig. 16: “Argyris” sequence: Hausdorff distance  $H_5$  ( $\downarrow$ ) along time.

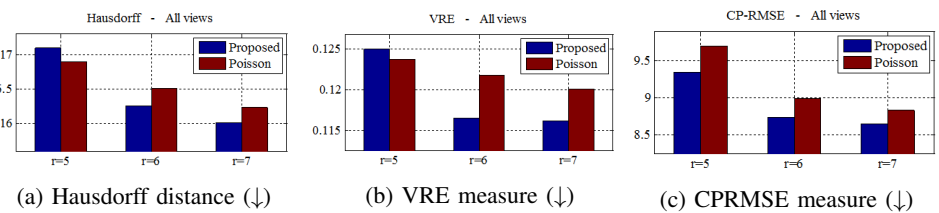


Fig. 17: “Argyris” sequence: Reconstruction performance, considering the mean for all views. The results for the employed and the “Poisson” method are given, with respect to reconstruction resolution.

evaluation methodology of section III-E, b) to showcase however its validity, and obviously c) evaluate the employed 3D reconstruction method, presenting also comparative results.

Fig. 15 presents two examples of “reconstructed” depthmaps versus the corresponding captured maps. As explained in section III-E, such pairs constitute the input to the proposed evaluation metrics. From Fig. 15(a) one can notice that the reconstructed silhouette(ii) is well-shaped and smooth, while the corresponding ground-truth (captured) silhouette(i) is noisy by nature, since it comes from sensor data. This means that, the evaluation method is practically limited by the non-perfect ground-truth assumption. More importantly, theoretically the evaluation methodology assumes perfect temporal synchronization and calibration of the sensors. In practice, not perfectly synchronized data from multiple sensors and/or small registration misalignments will lead to worse performance metric values. In other words, the evaluation method addresses the capturing-reconstruction process as a whole. If the capturing process is “noisy”, the method’s capability to differentiate a good reconstruction method from a bad one, is reduced. However, as demonstrated below, the method presents meaningful results.

In order to assist the reader, the symbols ( $\uparrow$ ) or ( $\downarrow$ ) are used in all subsequent figures, to highlight whether a higher or lower metric value, respectively, reflects better performance. The evolution of the Hausdorff distance metric along time, when the sensor  $c_5$  is employed for ground truth, is depicted in Fig. 16. During the first half of the sequence, the metric remains in low levels, whereas it increases during the second half due to fast motion of the user and loose inter-Kinect synchronization. Some strong peaks, as the highlighted one, correspond to missing-limb cases, as the one shown in Fig. 15(b). In accordance to section III-E1, the Hausdorff distance in this case is equal to the length of the missing limb, that is approximately 25 pixels.

Figure 17 depicts the mean values (considering all ground-truth views  $c_k$ ) for the metrics that reflect the volume/geometry reconstruction quality. The results are given for voxel-grid resolutions  $r = 5, 6$ , and  $7$ , considering the employed and the “Poisson” reconstruction method. All metrics decrease, as the reconstruction resolution increases, as expected. In all plots, the employed reconstruction method presents similar or slightly better performance than the “Poisson” method. This is explained by the doubled resolution along  $Y$  for the employed method. Only for low resolution ( $r = 5$ ), and according to VRE and Hausdorff distance, the Poisson method performs

better.

The Hausdorff distance for two views ( $c_0$  and  $c_2$ ) are given in Fig. 18. The same conclusions can be drawn. An additional conclusion is that the metric values for view  $c_2$  are higher, as expected, since sensor  $c_2$  does not participate in the reconstruction process.

Finally, results with respect to the RGB appearance quality are given in Fig. 19, using the structure similarity index (WMS3IM) metric. The color-per-vertex representation approach is compared with the UV texture-mapping approach, considering three reconstruction resolutions. The results are meaningful, since i) WMS3IM improves as the resolution increases; ii) the color-per-vertex representation always performs worse, since it produces blurred (lower resolution) rendered views than the originally captured one; iii) On the other hand, the UV texture-mapping approach performs well even at  $r = 5$ , since it directly maps the high-definition captured RGB textures. Finally, the WMS3IM values at the left diagram are higher than those at the right, since sensor  $c_0$  participates in the reconstruction and texture-mapping process.

### C. Volume-based motion tracking

Our motion capturing system is evaluated mainly using a dataset of Gaelic and Basque Traditional Sports, provided by the project RePlay. The specific dataset was selected for experimentation because, apart from multiple Kinect skeleton data, Vicon marker-based ground-truth is available. The 15-joints skeleton structure, extracted by the proposed method, constitutes a subset of the Kinect and Vicon structures and therefore, there exist one-to-one joint correspondences between the three structures. The captured motions are challenging, fast, with severe self-occlusions and simultaneous movements of several body parts. Sequences from different sport skill captures were chosen, characterized by short, quick movements. The data used in the experiments, can be found at <http://vcl.iti.gr/3dTl/TCSVT/dataset>.

An illustrative skeleton-tracking example is given in Fig. 20. As can be seen at the top figure, the estimates of the proposed method may be inaccurate at the presence of large reconstructed objects (e.g. the ball) touching the human limbs. This limitation is expected to be overridden by fusing in our method data from an inertia measurement unit. The plot diagram at the bottom of Fig. 20 depicts the estimated anthropometric angle (between two bones) along time for the most important limb of this “skill”. The valley of the curves at the beginning of the sequence corresponds to the flexion

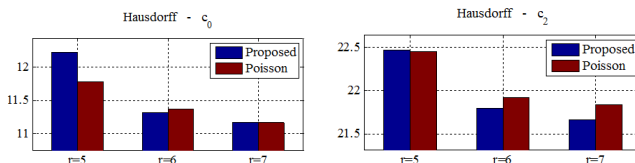


Fig. 18: “Argyris” sequence: Hausdorff distances  $H_k$  ( $\downarrow$ ) considering sensors  $c_k, k = \{0, 2\}$ .

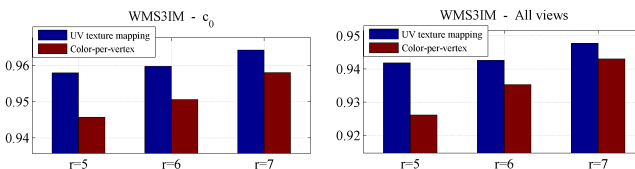


Fig. 19: “Argyris” sequence: WMS3IM similarity index ( $\uparrow$ ) considering sensor  $c_0$  (left) and all sensors (right). The results for the color-per-vertex representation and UV texture mapping are given.

of the knee for kicking. Whereas Kinect2 loses tracking for a few frames after the fast knee flexion (large valley that reaches  $0^\circ$ ), the proposed method tracks well the motion.

Table III shows comparisons of the angle estimates with the ground-truth, using the RMSE and the Mean Absolute Error (MAE) ( $\downarrow$ ), while highlighting with bold the most important limb, as analyzed by biomechanical engineers.

#### Runtime Evaluation

The experiments ran on a PC with an Intel Core i7 processor at 3.5 GHz, 16MB RAM and the NVidia GTX 680 graphics card. The proposed skeleton-tracking method can achieve frame rates higher than 10fps. a) The human-body volumetric function is reconstructed on the GPU at a volume resolution  $r = 6$  within approximately 20msec (see also V-A); b) The processing time for volume binarization and skeletonization, running on a CPU thread, is 10msec; c) Creating and processing the skeletal graph lasts 30 ms; d) Fitting a skeleton to the graph requires less than 10 ms. Although the implementation of the method after the volume extraction is not optimized, it allows the skeleton estimation at rates higher than 10fps.

#### VI. CONCLUSIONS-FUTURE WORK

In this work, the main elements of an integrated system that targets real-time future 3D applications were described, including multi-Kinect2 capturing and fast 3D reconstruction of moving humans, as well skeleton-based motion tracking from multiple depth cameras. Regarding these elements, novel approaches were proposed and/or the adaptation of existing ones were described. Simultaneously, a novel framework for the quantitative evaluation of 3D reconstruction systems has been proposed.

Some limitations of the ongoing, in terms of research and development, system have also been discussed. Overriding these limitations is subject of ongoing research: Regarding the non-perfect synchronization issue with consumer-grade RGB-D sensors, which may deteriorate the reconstruction quality

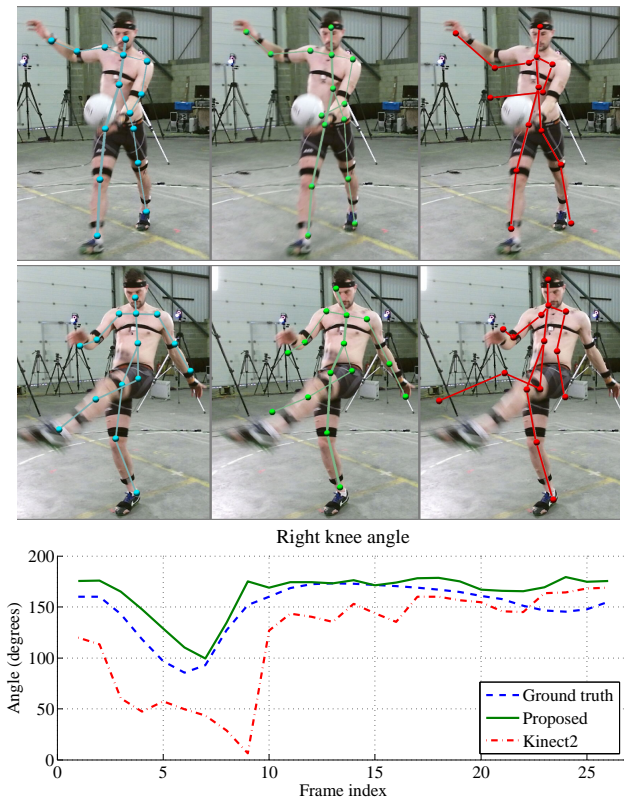


Fig. 20: Gaelic Football Punt Kick. Qualitative and quantitative skeleton-tracking results: Ground-truth (Vicon) with cyan, proposed with green and Kinect2 (using the best skeleton among the 4 Kinect2 sensors) with red.

TABLE III: Skeleton tracking results: Mean errors between the estimated angle and the ground-truth.

Sequences	Left Elbow	Right Elbow	Left Knee	Right Knee				
Kinect2	MAE	RMSE	MAE	RMSE	MAE	RMSE	MAE	RMSE
Jai Alai (Sidearm Shot)	31.19	35.69	<b>25.96</b>	<b>38.35</b>	22.58	30.68	12.99	18.22
Pelota (R-H Serve)	40.35	48.04	<b>29.30</b>	<b>38.92</b>	3.43	8.34	14.88	20.04
Handball (R-H Volley)	38.62	45.71	<b>34.06</b>	<b>46.54</b>	13.71	26.06	7.74	18.38
Gaelic Football (R-F Punt Kick)	5.39	10.42	25.084	25.79	18.34	20.53	<b>21.03</b>	<b>53.11</b>
Proposed								
Jai Alai (Sidearm Shot)	25.29	29.34	<b>14.26</b>	<b>21.60</b>	9.940	13.68	12.87	18.11
Pelota (R-H Serve)	16.79	25.59	<b>16.39</b>	<b>25.09</b>	9.30	19.41	9.04	16.29
Handball (R-H Volley)	17.78	26.51	<b>14.65</b>	<b>23.35</b>	7.15	17.51	10.014	25.31
Gaelic Football (R-F Punt Kick)	16.34	26.47	23.37	31.42	15.88	17.32	<b>10.85</b>	<b>17.20</b>

in fast motion, we work towards spatio-temporal interpolation via estimation of the separate 3D data misalignment. With respect to the skeleton tracking method, limitations regarding topology change (e.g. “piece hands together”) are expected to be overridden by a skeleton-fitting scheme, where the limbs of a user-specific skeleton model are fitted to the extracted MST. Additionally, by splitting the rigid-body part into upper and lower segments and fusing in our method data from two inertial measurement units, we aim at handling the limitations due to the assumption that the trunk joints move rigidly.

To increase realism, with respect to 3D reconstruction of humans, a generic future-work direction is the improvement of the visual quality and frame-rates, by continuously investigating towards more efficient solutions. For example, in many applications the reconstruction of user's face is more important than other body parts, and therefore we investigate towards the real-time deformation and fusion of a pre-scanned user's head model with the captured 3D data. In real-time applications, such as Tele-Immersion, both i) realistic replications of the users appearance (heavy data) and ii) natural interaction among geographically remote user (real-time exchange of the 3D reconstructions among remote locations), are required. The above contradiction also highlights the need to research both in the compression of the 3D replicants, and in the network layer to offer novel tele-immersion architectures, allowing to scale up the interaction among large number of users capable to support such exciting applications.

#### ACKNOWLEDGMENT

This work was supported by the EU funded project PATH-way under contract 643491.

#### REFERENCES

- [1] R. Vasudevan, G. Kurillo, E. Lobaton, T. Bernardin, O. Kreylos, R. Balajsy, and K. Nahrstedt, "High quality visualization for geographically distributed 3D teleimmersive applications," *IEEE Trans. on Multimedia*, vol. 13, no. 3, June 2011.
- [2] A. Doumanoglou, D. Alexiadis, D. Zarpalas, and P. Daras, "Towards real-time and efficient compression of human time-varying-meshes," *IEEE Trans. on Circuits and Systems for Video Technology*, 2014.
- [3] S. Crowle, A. Doumanoglou, B. Poussard, M. Boniface, D. Zarpalas, and P. Daras, "Dynamic adaptive mesh streaming for real-time 3D teleimmersion," in *20th Int. Conf. on Web 3D Technology*, Crete, 2015.
- [4] P. Fechteler, A. Hilsmann, P. Eisert, S. V. Broeck, C. Stevens, J. Wall, M. Sanna, D. A. Mauro, F. Kuijk, R. Mekuria, P. Cesari, D. Monaghan, N. O'Connor, P. Daras, D. Alexiadis, and T. Zahariadis, "A framework for realistic 3D tele-immersion," in *Mirage, 6th Int. Conf. on Comp. Vision/Comp. Graph. Collaboration Techniques and Appl.*, Berlin, 2013.
- [5] J.-S. Franco and E. Boyer, "Efficient polyhedral modeling from silhouettes," *IEEE Trans. Pattern Anal Mach. Intell.*, vol. 31, no. 3, 2009.
- [6] G. Vogiatzis, C. Hernandez, P. Torr, and R. Cipolla, "Multiview stereo via volumetric graph-cuts and occlusion robust photo-consistency," *IEEE Trans. Pattern Anal Mach. Intell.*, vol. 29, no. 12, pp. 2241–2246, 2007.
- [7] Y. Furukawa and J. Ponce, "Carved visual hulls for image-based modeling," *Int. Journal of Computer Vision*, vol. 81, pp. 53–67, 2009.
- [8] J. Carranza, C. Theobalt, M. A. Magnor, and H.-P. Seidel, "Free-viewpoint video of human actors," *ACM Transactions on Graphics*, vol. 22, no. 3, pp. 569–577, 2003.
- [9] E. de Aguiar, C. Stoll, C. Theobalt, N. A. H.-P. Seidel, and S. Thrun, "Performance capture from sparse multi-view video," *ACM Transactions on Graphics*, vol. 27, no. 3, 2008.
- [10] J. Gall, B. Rosenhahn, T. Brox, and H.-P. Seidel, "Optimization and filtering for human motion capture: A multi-layer framework," *Int. Journal of Computer Vision*, vol. 87, no. 1, pp. 75–92, 2010.
- [11] G. Turk and M. Levoy, "Zippered polygon meshes from range images," in *SIGGRAPH '94*, 1994, pp. 311–318.
- [12] B. Curless and M. Levoy, "A volumetric method for building complex models from range images," in *SIGGRAPH '96*, 1996.
- [13] D. Alexiadis, D. Zarpalas, and P. Daras, "Real-time, full 3-D reconstruction of moving foreground objects from multiple consumer depth cameras," *IEEE Trans. on Multimedia*, vol. 15, pp. 339–358, Feb. 2013.
- [14] ——, "Real-time, realistic full-body 3D reconstruction and texture mapping from multiple kinects," in *Proc. IEEE IVMSP*, June 2013.
- [15] A. Maimone and H. Fuchs, "Real-time volumetric 3D capture of room-sized scenes for telepresence," in *IEEE 3DTV-Conference*, 2012.
- [16] M. Kazhdan, M. Bolitho, and H. Hoppe, "Poisson surface reconstruction," in *Proc. 4th Eurographics symp. on Geometry processing*, 2006.
- [17] M. Kazhdan, "Reconstruction of solid models from oriented point sets," in *Proc. 3rd Eurographics symposium on Geometry processing*, 2005.
- [18] A. Maimone and H. Fuchs, "Encumbrance-free telepresence system with real-time 3D capture and display using commodity depth cameras," in *Proc. IEEE ISMAR*, 2011.
- [19] A. Maimone, J. Bidwell, K. Peng, and H. Fuchs, "Enhanced personal autostereoscopic telepresence system using commodity depth cameras," *Computers and Graphics*, vol. 36, no. 7, pp. 791–807, 2012.
- [20] R. Newcombe, D. Fox, and S. Seitz, "DynamicFusion: Reconstruction and tracking of non-rigid scenes in real-time," in *CVPR*, 2015.
- [21] R. A. Newcombe, S. Izadi, O. Hilliges, D. Molnyneux, D. Kim, A. J. Davison, P. K. and Jamie Shotton, S. Hodges, and A. W. Fitzgibbon, "KinectFusion: Real-time dense surface mapping and tracking," in *Proc. 10th IEEE ISMAR*, 2011, pp. 127–136.
- [22] E. Lachat, H. Macher, M.-A. Mittet, T. Landes, and P. Grussenmeyer, "First experiences with kinect v2 sensor for close range 3D modelling," *Int. Archives of the Photogrammetry, Remote Sensing and Spatial Inf. Sciences*, vol. XL-5/W4, pp. 93–100, 2015.
- [23] H. Hisahara, S. Hane, H. Takemura, Y. Chin, T. Ogitsu, and H. Mizoguchi, "3D point cloud-based virtual environment for safe testing of robot control programs: Measurement range expansion through linking of multiple Kinect v2 sensors," in *6th International Conference on Intelligent Systems, Modelling and Simulation (ISMS)*, February 2015.
- [24] M. Kowalski, J. Naruniec, and M. Daniluk, "Livescan3D: A fast and inexpensive 3D data acquisition system for multiple Kinect v2 sensors," in *International Conference on 3D Vision (3DV)*, October 2015.
- [25] M. Ye, X. Wang, R. Yang, L. Ren, and M. Pollefeys, "Accurate 3D pose estimation from a single depth image," in *IEEE ICCV*, 2011.
- [26] J. Shotton, A. Fitzgibbon, M. Cook, T. Sharp, M. Finocchio, R. Moore, A. Kipman, and A. Blake, "Real-time human pose recognition in parts from a single depth image," in *IEEE CVPR*, 2011.
- [27] B. Michoud, E. Guillou, and S. Bouakaz, "Real-time and markerless 3D human motion capture using multiple views," in *Human Motion Understanding, Modeling, Capture and Animation*, ser. LNCS, 2007.
- [28] S. M. Yoon, M. Cornelius, and G. Holger, "3D skeleton extraction from volume data based on normalized gradient vector flow," in *WSCG '09*, 2009, pp. 177–182.
- [29] J. Cao, A. Tagliasacchi, M. Olson, and H. Zhang, "Point cloud skeletons via Laplacian based contraction," in *Shape Modeling Int. Conf.*, 2010.
- [30] S. Matthias, H. Stefan, R. Matthias, and B. Horst, "Skeletal graph based human pose estimation in real-time," in *British Machine Vision Conference (BMVC)*, 2011.
- [31] H. Sarbolandi, D. Lefloch, and A. Kolb, "Kinect range sensing: Structured-light versus time-of-flight kinect," *Computer Vision and Image Understanding*, vol. 139, pp. 1–20, Oct. 2015.
- [32] D. G. Lowe, "Object recognition from local scale-invariant features," in *Int. Conf. on Computer Vision*, vol. 2, 1999, pp. 1150–1157.
- [33] D. G. A. Kendall, "Survey of the statistical theory of shape," *Statistical Science*, vol. 4, no. 2, pp. 87–99, 1989.
- [34] V. A. Epanechnikov, "Non-parametric estimation of a multivariate probability density," *Theory Probab. Appl.*, vol. 14, no. 1, pp. 153–158, 1969.
- [35] W. E. Lorensen and H. E. Cline, "Marching cubes: A high resolution 3D surface construction algorithm," *Comp. Graphics*, vol. 21(4), 1987.
- [36] D. P. Huttenlocher, G. A. Klanderman, G. A. Kl, and W. J. Rucklidge, "Comparing images using the hausdorff distance," *IEEE Trans. Pattern Anal Mach. Intell.*, vol. 15, pp. 850–863, 1993.
- [37] Z. Wang and A. C. Bovik, "Mean squared error: love it or leave it? a new look at signal fidelity measures," *IEEE Signal Processing Magazine*, vol. 26, no. 1, pp. 98–117, 2009.
- [38] Z. Wang, A. C. Bovik, H. R. Sheikh, and E. P. Simoncelli, "Image quality assessment: from error visibility to structural similarity," *IEEE Trans. on Image Processing*, vol. 13, no. 4, pp. 600–612, 2004.
- [39] Z. Wang and Q. Li, "Information content weighting for perceptual image quality assessment," *IEEE Trans. on Image Processing*, vol. 20, no. 5, pp. 1185–1198, 2011.
- [40] Z. Wang, E. P. Simoncelli, and A. C. Bovik, "Multiscale structural similarity for image quality assessment," in *37th IEEE Asilomar Conference on Signals, Systems and Computers*, 2003.
- [41] T.-C. Lee, R. L. Kashyap, and C.-N. Chu, "Building skeleton models via 3-D medial surface/axis thinning algorithms," *CVGIP: Graph. Models Image Process.*, vol. 56, no. 6, pp. 462–478, 1994.
- [42] Slemenda, W. Charles, S. L. Hui, C. J. Williams, J. C. Christian, F. J. Meaney, and C. C. Johnston, "Bone mass and anthropometric measurements in adult females," *Bone and mineral*, 1990.
- [43] J. C. Gower and G. J. S. Ross, "Minimum spanning trees and single linkage cluster analysis," *Journ. of the Royal Statistical Society*, 1969.
- [44] S. Shantaiya, K. Verma, and K. Mehta, "Multiple object tracking using kalman filter and optical flow," *European Journal of Advances in Engineering and Technology*, vol. 2, no. 2, pp. 34–39, 2015.